PAPER

Check for updates

A robust protonic ceramic fuel cell with a triple conducting oxygen electrode under accelerated stress tests

Shuanglin Zheng,[a] Wenjuan Bian [ID][b] and Hanping Ding [ID]*[a]

Developing protonic ceramic fuel cells is regarded as a promising approach for the electrochemical conversion of the chemical energy in hydrogen to power with high efficiency. Lowering the operating temperature can accelerate its application by integrating more reliable stack components to enable long-term durability. One critical pathway is to facilitate the oxygen reduction reaction *via* developing triple conducting oxygen electrodes for increasing active sites for catalysis and charge transport in bulk and interface, aiming to improve reaction kinetics. In this work, the recently developed triple conducting oxygen electrode $PrNi_{0.7}Co_{0.3}O_{3-\delta}$ has been examined under dynamic operating conditions to understand the degradation behaviors through an accelerated stress test. Various test protocols have been employed to measure and compare the mechanical and electrochemical performances under different dynamic parameters and thermal cycling conditions. The results strongly indicate that the as-fabricated cells exhibit a high level of endurance despite a slightly increased polarization resistance and an accelerated stress test is an effective way to examine cell reliability under more dynamic kinetics.

Introduction

Protonic ceramic electrochemical cells have been increasingly considered as a promising technology to achieve the carbon-neutral energy cycle *via* direct conversion of renewable power into hydrogen.[1–4] In the fuel cell mode, the chemical energy in stored hydrogen is effectively transformed into a new form of power, with water being the only byproduct. This process avoids carbon emissions.[5–7] Compared with conventional oxide-ion conducting solid oxide fuel cells, protonic ceramic fuel cells (PCFCs) undoubtedly deliver technical advantages such as lower operating temperature, cheaper system cost, and reliable operation.[8–11] The recent progress on materials, performances, and stack development has demonstrated their great potential for being operated with fuel flexibility and robustness in electricity generation.[12–15]

As reducing operating temperature can significantly improve material compatibilities and cost-effectiveness of stack manufacturing, considerable endeavors have been made to enhance the performance of materials in the temperature range of 400 °C–600 °C and ensure their long-term stability.[16–19]

However, the sluggish reaction kinetics of oxygen electrodes leads to the remaining technical challenges in pursuit of suitable electrode compositions for the water splitting reaction. To overcome this rate-limiting step, developing a triple conducting electrode is considered as an effective approach to extend active reaction sites throughout the entire electrode surface and interface for accelerating the kinetics of oxygen evolution and proton transfer.[20–23] There have been several examples of triple conducting oxide (TCO) materials being developed, demonstrating significant proton conductivity and improved cell performance by increasing the reaction efficiency of both the hydrogen oxidation reaction (HOR) and the oxygen reduction reaction (ORR) at triple phase boundaries (TPBs).[24–27] $PrBa_{0.5}Sr_{0.5}Co_{2-x}Fe_xO_{5+\delta}$ ($x = 0$, 0.5 and 1.0), one promising layered perovskite, was compounded to promote electrochemical active sites, realizing lower area specific resistance (ASR), 0.33 Ω cm^2 at 500 °C and 0.056 Ω cm^2 at 600 °C, than $Ba_{0.5}Sr_{0.5}Co_{0.8}Fe_{0.2}O_{3-\delta}$ at similar temperature (0.70 Ω cm^2 at 500 °C).[24,25] These doped variants demonstrated the intensified oxygen bulk diffusion and surface exchange. $BaCo_{0.4}Fe_{0.4}Zr_{0.1}Y_{0.1}O_{3-\delta}$, another TCO material, was based on a material family of proton conducting electrolytes with intrinsic proton formation properties, resulting in a significant improvement in the overall performance of the cell.[26–28] Some other examples also include a group of unique La–Ni based layered perovskites, recognized as Ruddlesden–Popper oxides, $La_{n+1}Ni_nO_{3n+1}$, being selected as an alternate material for the

[a] *School of Aerospace and Mechanical Engineering, University of Oklahoma, Norman, OK 73019, USA. E-mail: hding@ou.edu*

[b] *Department of Hydrogen and Electrochemistry, Idaho National Laboratory, Idaho Falls, ID 83415, USA*

cathode. $Pr_{1.75}Ba_{0.25}NiO_{4+\delta}$ and $Pr_{1.2}Sr_{0.8}NiO_{4+\delta}$, with different substitution at the A-site, both exhibited triple mixed conductivity. The dispersion of extra oxygen ions in the interstitials can enhance ionic transport, thus yielding oxygen exchange properties as well as hydration.[29–32]

We have recently demonstrated a perovskite-structured $PrNi_xCo_{1-x}O_{3-\delta}$ (PNC) oxide as a TCO oxygen electrode for electrochemical cells in the operation of a fuel cell or an electrolysis cell.[33,34] This PNC electrode can function as the oxygen electrode (cathode) featuring high efficiency and stability, hence avoiding any need for doping with alkaline earth metals such as calcium, strontium, and barium for higher activity. Although the doping of these elements to increase the ionic conductivity and accelerate ORR kinetics is undebatable, the tendency for enrichment and segregation at interfaces often results in further exacerbation by the presence of carbon dioxide and water vapor. Moreover, a higher level of hydration ability makes the proton defect concentration significantly increased, which is a contributing factor to triple conduction. The density functional theory calculation also indicated the reduction of barrier energy favorable for proton conduction.[35–39] This electrode has demonstrated excellent electrochemical activity for both the ORR and water oxidation reaction in fuel cell and electrolysis modes due to several factors: high oxygen vacancy concentration, highly triggered proton conductivity from the hydrated lattice, and low thermal expansion coefficient. After integration into $BaZr_{0.4}Ce_{0.4}Y_{0.1}Yb_{0.1}O_{3-\delta}$ (BZCYYb4411) electrolyte based cells, it exhibited peak power density of 0.53 W cm^{-2} at 600 °C in the fuel cell mode and 1.31 A cm^{-2} at 1.40 V and 600 °C in the electrolysis mode respectively, which were ranked among the highest performances.[40] In order to achieve a balance between activity and thermal properties, this material system has undergone additional optimization via the examination of a range of compositions regarding $PrNi_xCo_{1-x}O_{3-\delta}$ (x = 0.1, 0.3, 0.5, 0.7, and 0.9) with different Ni/Co ratios to find the optimal composition. It was revealed that $PrNi_{0.7}Co_{0.3}O_{3-\delta}$ (PNC73) showed exceptional performance and adjusted thermal matching properties with the electrolyte. The electrolysis current density reached up to 1.48 A cm^{-2} at 1.3 V and a peak power density of 0.95 W cm^{-2} was achieved at 600 °C, exceeding the performance of the PNC55 electrode by 80%. This electrode also showed satisfactory output (0.14 W cm^{-2}) when the temperature was reduced to 350 °C.[33,34]

To further validate the feasibility of this PNC73 electrode in a PCFC system, the evaluation of long-term stability in the operation mode is very critical, which is essential for scaling up and commercialization.[41–44] The accelerated stress test is an effective method to examine the robustness of cell properties by challenging the adaptability of materials and interfaces upon dynamic changes of testing conditions. In this work, we have performed a series of accelerated stress tests on single cells with the BCZYYb4411 electrolyte and PNC73 oxygen electrode. Our results have preliminarily demonstrated that the electrochemical performances are robust against dynamical stress operations, which is attributed to the enhanced interface bonding strength.

Results and discussion

Characterization on the cell microstructure

As shown in Fig. 1a, the fresh sandwich-structured single cell has three layered components which are intimate without any visible defects. The interfaces between the electrolyte and electrode exhibit strong bonding. After the transient cycling test, the observation reveals that each layer, spanning from the electrode to the electrolyte, remains flat and firmly attached, owing to the exceptional bonding strength (Fig. 1b). Although the thickness of the cathode slightly shrank from 17.8 μm to 12.7 μm (by less than 30%), the dominant cathode layer, PNC73, was preserved in fine grain shape, resulting in effective gas permeability and ion transport. After the test, the cathode/electrolyte interface didn't show any crack, delamination or other defect (Fig. 1c), which is attributed to the less difference in the thermal expansion coefficient (TEC) between PNC73 and electrolyte than other variants of PNC series material, which resulted in enhanced mechanical compatibility. After being tested at dynamic voltages, the grains of the PNC73 cathode are consistently durable with adequate pores allowing enough air flow through it, ensuring the prerequisite of the ORR. Due to the high density of BZCYYb4411, the anode layer exhibits a similar dense pattern to the electrolyte but with reasonable porosity after reducing and subsequent operation at dynamic applied voltage, which is concluded as a reliable substrate support featuring tolerable mechanical strength and efficient gas channels as well as triple-conducting paths (Fig. 1d).[33,34,40]

Electrochemical performances on the stability of a durable triple-conducting electrode

Step-voltage tests and transient cycling tests, which include the consistent alteration and random transiency of applied voltage on full cells, have been used to evaluate the consistency of electrochemical performance.[45–47] As the test at the steady state could effectively demonstrate the durability of structures, materials, and interfaces, some dynamic conditions such as
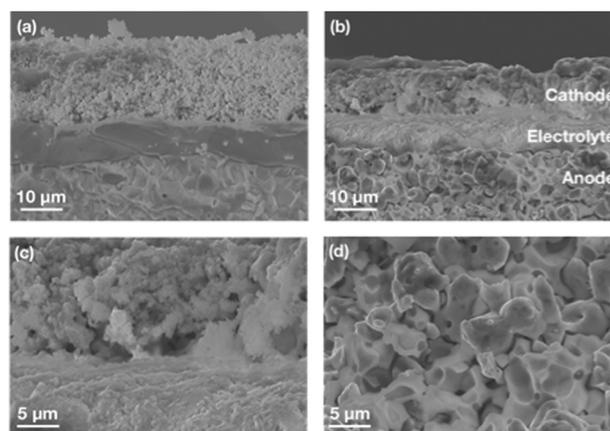

Fig. 1 Observation of the microstructure in a PCFC single cell (PNC73-electrode/BZCYYb-electrolyte/NiO-BZCYYb-support) before or after the durable operation: (a) as-prepared fresh cell without reduction; (b)–(d) cross section view of the cell after second-transient-cycling at 600 °C.
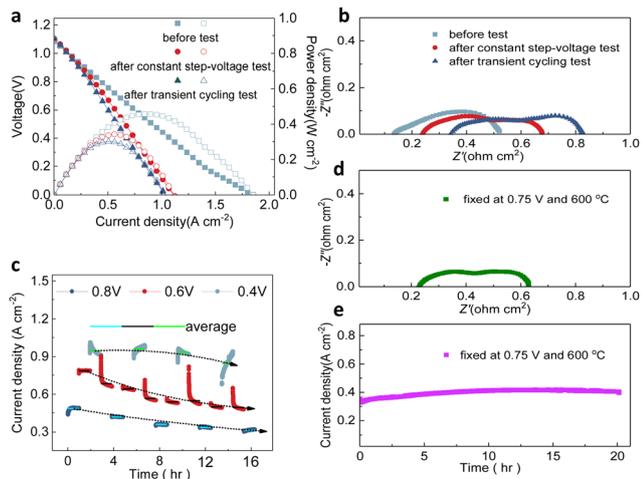
Fig. 2 Electrochemical performance of a PNC73/BZCYYb/NiO-BZCYYb fabricated cell in the fuel cell mode. (a) and (b) Comparison on the *I–V* curve, *I–P* curve and EIS of before test samples and after step-voltage/transient test samples. (c) Constant step-voltage of 0.2 V test at 600 °C. (d) and (e) Stability test of the cell at a constant voltage of 0.75 V and 600 °C for 20 h.

thermal shock and changed current density or voltage could challenge the cells. Moreover, it has been considered that the dynamic operation could be counted as the accelerated stress test for predicting the cell durability in a more reasonable manner compared to the steady state.[48–50] Furthermore, to elaborate the potential effect of transient operations, several different transient cycling tests were conducted to validate the robustness of fabricated PNC73 full cells.

Fig. 2a demonstrates the main comparisons of the electrochemical performance of the cell operating at 600 °C in the fuel cell mode with pure hydrogen as fuel after different transient test modes as shown later in Fig. 3. First, the open circuit voltage (OCV) of the cell is 1.08 V before any test, and 1.10 V after the step voltage test and transient voltage test, which are close to the theoretical potential value (1.13 V) calculated using the Nernst equation. This result proved that the electrolyte membrane is very dense and excellently sealed. Furthermore, the *I–V* curves yield no drastic non-linear fluctuation, confirming that the interior structure of lanthanide nickelates is little compromised. The peak power densities are 457 mW cm^{-2} before the test, 342 mW cm^{-2} after the step voltage test and 302 mW cm^{-2} after the transient test, respectively. Though peak power densities have been decreased by 33% and 51% in two distinguished stressed modes separately, they are still competitive among other cathode materials. More specifically, the performance (302 mW cm^{-2} at 600 °C after the transient test) has been approximately three times higher than the cell with selected rhombohedral phase La$_{0.7}$Sr$_{0.3}$Mn$_{0.7}$Ni$_{0.3}$O$_{3-\delta}$ (LSMN7373) as the cathode (102 mW cm^{-2} at 600 °C) and similar to the peak power density of cubic phase LSMN7373 (386 mW cm^{-2} at 600 °C), which has been highlighted.[51] More work related to other cathode components, such as (La$_{0.6}$Sr$_{0.4}$)$_{0.95}$-Co$_{0.2}$Fe$_{0.8}$O$_{3-\delta}$, consistently showed lower peak power density
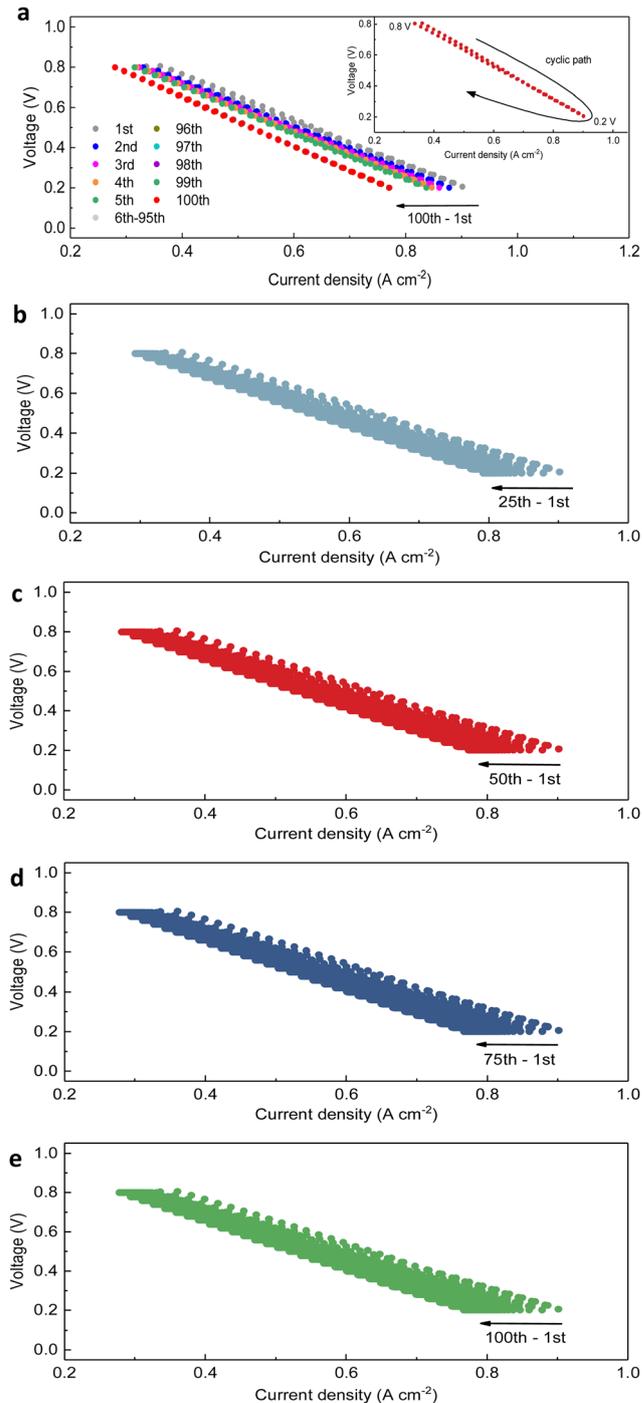

Fig. 3 The dynamic cycling test for examining the stability of components and interface: Transient cycling tests of the PNC73 full cell at 0.8 V and 0.2 V for 100 cycles in the fuel cell mode at 600 °C. (a) *I–V* curve of 1–100 cycles. (b)–(e) Sub-grouped *I–V* curves: 1st–25th cycle; 1st–50th cycle; 1st–75th cycle and 1st–100th cycle.

(214 mW cm^{-2} at 600 °C), all verifying the potent capability to maintain the efficient ORR activity occurring at the interface and substantial triple-conducting paths are preserved, then shedding light on the long-term cell use or operation under extreme electrochemical conditions.[52] As indicated in the

impedance spectra (Fig. 2b), though the ohmic resistance R_o has recognizable escalation, ranging from 0.13 Ω cm^2 to 0.23 Ω cm^2 and then increases to 0.34 Ω cm^2 correspondingly, the polarization resistance R_p of each cell sample is close to 0.44 Ω cm^2 (0.39 Ω cm^2, 0.45 Ω cm^2 and 0.48 Ω cm^2, respectively), denoting no sharp increment and assuring that every layer of full cells has been well-functional with continuous current flowing. It should be noted that this temporary degradation on current density or polarization resistance will be relieved after the dynamic operation is terminated for a while.

For a detailed constant step-voltage test, the applied potential on full cells has been altered from 0.8 V to 0.6 V and then to 0.4 V, from high to low and then back forth with certain changing patterns, and the duration of each stagnant-voltage was 1 h, repeated for 17 cycles at unchangeable 600 °C (Fig. 2c). It is apparently noted that, when applied with potential 0.4 V for four intermittent cycles, the current density of each cycle has been clustered around 0.92 A cm^{-2} but also with the analytical fluctuation range of 0.14 A cm^{-2}. Resembling tendency is witnessed while altering the applied potential to another two pre-set values, the current density converges at 0.38 A cm^{-2} for 0.8 V and 1.5-fold increased value (0.59 A cm^{-2}) for 0.6 V. Additionally, the cell stability, in terms of step-voltage shifting, has been further substantiated through the mean value of current density for each cycling duration. For instance, the average current densities of four cycles at 0.4 V are 0.94 A cm^{-2}, 0.96 A cm^{-2}, 0.94 A cm^{-2} and 0.84 A cm^{-2} (green solid lines as indicated); comparably, the average values of eight cycles at 0.6 V are 0.79 A cm^{-2}, 0.68 A cm^{-2}, 0.64 A cm^{-2}, 0.57 A cm^{-2}, 0.54 A cm^{-2}, 0.55 A cm^{-2}, 0.50 A cm^{-2} as well as 0.49 A cm^{-2} (black solid lines as indicated), and the mean ones of five patterns at 0.8 V are 0.31 A cm^{-2}, 0.34 A cm^{-2}, 0.36 A cm^{-2}, 0.42 A cm^{-2} and 0.48 A cm^{-2} (blue solid lines as indicated). The slightly downscaling current density is irrefutable under long time stressed tests due to oxygen starvation and possibly some stress-induced electrode interface deterioration.

Predominantly, the dashed trendlines in Fig. 2c also indicate the insignificant variation in cell performance for inconsistent voltage restrictions, resulting in exceptional durability under step-voltage conditions. When a 0.8 V input voltage was applied, the current density decreased marginally from 0.48 A cm^{-2} in the first cycle to 0.31 A cm^{-2} in the fifth cycle. Similarly, at 0.6 V and 0.4 V, the current density reduced to 0.49 A cm^{-2} in the eighth cycle and 0.84 A cm^{-2} in the fourth cycle, respectively. This non-equilibrium response is common to some degree, and it is not very clear to identify the certain reasons. However, it is indisputable that the current densities obtained even at the end of step-voltage tests approximately were close to 0.50 A cm^{-2}, which was just over the cells using PrBa$_{0.5}$Sr$_{0.5}$Co$_2$O$_{5+\delta}$ as the cathode.[53] The steady current density at high input voltage remained around 0.31 A cm^{-2}, which is surprisingly higher than that of full cells using certain PNC series electrodes as PNC37 or PNC19.[33] As shown in Fig. 2d and e, the constant-voltage cell stability test has been conducted for 20 h when the cell was fixed at 0.75 V and 600 °C and the related

impedance spectrum has been collected. The result demonstrates the stable output under a steady condition instead of dynamic operation, which indicates that the dynamic operation is more useful to investigate the electrochemical behaviors.

The current density was initially 0.33 A cm^{-2}, and then it has gradually ramped up to 0.42 A cm^{-2} after the fuel cell experienced electrochemical conditions for 11 hours though it slightly dropped to around initial value at the end of 20 hours duration. In terms of functioning time, the current density of the PNC73 full cell fluctuated around 27%, which holds its stability for long-term working conditions. It is also worth mentioning that the R_o is 0.22 Ω cm^2 and R_p is 0.41 Ω cm^2, which are more closely aligned with the values of the cell before the transient tests in Fig. 2b. Therefore, we can conclude that the dynamic operation challenges the cell stability significantly, which is essential for evaluating PCFC stability.

The PNC73 full cell was thereafter subjected to the transient test by sweeping among a range of voltages. As presented in Fig. 3a, the results of the transient cycling test for 100 cycles, when the applied potential on the cell was between 0.8 V and 0.2 V, provide the information that there is an evident horizontal shift towards left with more cycles conducted. This showed some slight cell degradation with decreased current density, especially by comparing the first five cycles with the last five cycles. It is attributed to oxygen starvation, which is not a permanent degradation. Furthermore, the initial current density for the first transient test at 0.8 V was 0.36 A cm^{-2}, which definitely meets the criteria for downscaled performance in robustness testing. This was similarly observed for both 0.6 V and 0.4 V conditions. The subsequent results are derived from the comparison between the initial current density and instantaneously recorded values under each specific voltage and electrochemical conditions within the first transient test. When the applied voltage is regarded as the control variable, the maximum amount of variation in current density for 100 cycles is 0.09 A cm^{-2} for 0.2 V, while the minimum is 0.04 A cm^{-2} for 0.8 V. These findings confirm that the low applied voltage should be reduced in order to ensure the long-term durability of cells. After re-categorizing the I–V data, the results concerning four groups of 1st–25th, 1st–50th, 1st–75th and 1st–100th cycles are organized to display the analogous trend of cell performance on the mild downgrade (Fig. 3a–e). With each additional 25-cycle operation, the durability of the PNC73 full cell was further investigated. For instance, ar 0.6 V, the varying range of current density is 0.08 A cm^{-2} for the first 25 cycles, while that for the following three repetitions is 0.05 A cm^{-2}, 0.02 A cm^{-2} and 0.01 A cm^{-2} respectively, indicating that the output amount is trimming but generally stable and achieves vital durability until the last cycle. Furthermore, the I–V relationship of each transient cycle, as shown in Fig. 3b–e, is confirmed to be roughly linear and steady, confirming the integrity of layered-structures and stable interfaces on cells and holding consistency with results from SEM images. Clearly, while linking a similar downscaling shift among 1st–5th cycles with 96th–100th cycles, the current density has decreased more drastically in the early stages of cycling than in the last few

cycles. After explainable degradation proceeded, the cell performance tended to be determinate with certain sets of current density–voltage values, which was anticipated by previous electrochemical results.[54–56]

The step voltages applied have some negative effects on the full cell electrochemical performance, resulting in deterioration in current density. Later, we would discuss that these problems are temporary. Thus, the second transient cycling tests between 0.9 V and 0.2 V for 100 cycles in the fuel cell mode, but with different levels of applied voltages, 20 mV, 50 mV and 100 mV respectively, have been conducted. As shown in Fig. 4a–c, the comparison of the diminishing amount of current density (the horizontal shift on each curve) indicates that when the variation of step voltage was 100 mV, the ranges of current density were the largest, 0.06 A cm^{-2} for 0.2 V and 0.03 A cm^{-2} for 0.9 V. To clearly show one cycle, Fig. 5a shows the difference in current density at the same voltage, which indicates that the dynamic cycling would not easily yield the exactly same curves. In comparison, the ranges were 0.02 A cm^{-2} for 0.2 V and 0.03 A cm^{-2} for 0.9 V as the variation was 20 mV, whereas they were 0.02 A cm^{-2} for 0.2 V and 0.01 A cm^{-2} for 0.9 V as the
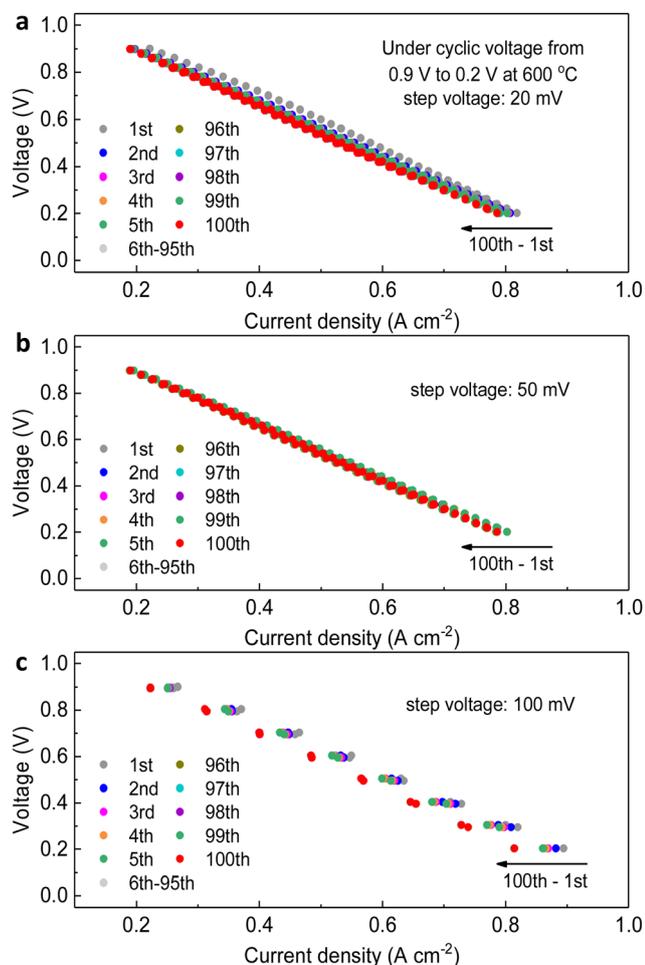

Fig. 4 Transient cycling tests of the PNC73 full cell at 0.9 V and 0.2 V for 100 cycles in the fuel cell mode at 600 °C in terms of different step-voltages. (a)–(c) *I–V* curves of 20 mV, 50 mV and 100 mV step voltages.
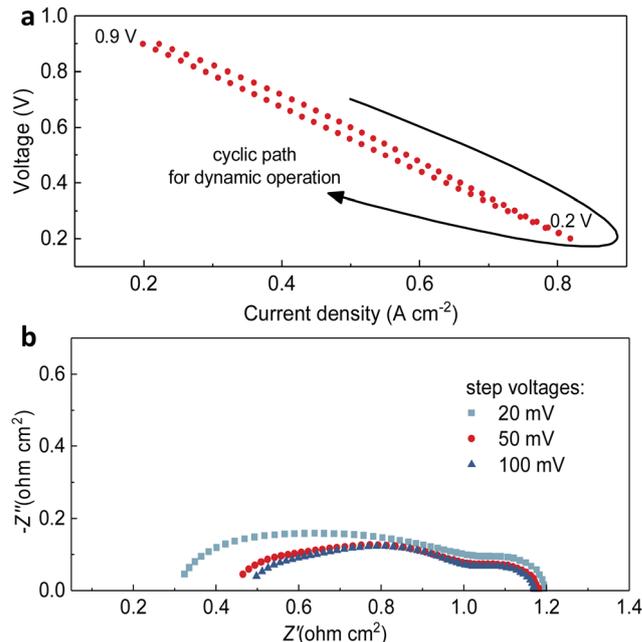

Fig. 5 Re-examination after transient cyclic tests: (a) a detailed demonstration of the cyclic path from 0.9 to 0.2 V. (b) EIS curves of the cell after the transient test with 20 mV, 50 mV and 100 mV step voltages.

variation was 50 mV. Although the result of degeneracy in cell performance is not negligible when the variation is 100 mV at 0.2 V and 600 °C, which is 0.06 A cm^{-2}, the shifts of current density under other testing conditions are validated to keep up steady cell performance with continual current generated. Similarly, when focusing on grey dots representing other cycles in between, it holds consistency of the marginally dropping pattern on current density to the lowest level of the ultimate cycle almost for all three settings. However, it is obvious that several middle cycles yielded weaker performance at 100 mV step voltage, which seems unseen before, but the current density varied in a certain range highly elucidates this unique dynamic stability. These shifts are the temporary phenomenon due to the oxygen starvation when the current density is dynamically changed, and the cell was not damaged by these operations.

The impedance spectra were collected after each cyclic test in Fig. 4, as shown in Fig. 5b. The maximum of R_o (0.50 Ω cm^2) belongs to the cell when the voltage change was 100 mV, followed by 0.32 Ω cm^2 for 20 mV and 0.47 Ω cm^2 for 50 mV, demonstrating that the larger shift of practicable voltage led to highly escalated ohmic resistance. However, the R_p of three testing procedures showed reverse pattern, that is, the R_p of the cell experienced changing voltage of 100 mV is the minimal 0.65 Ω cm^2, and they are 0.79 Ω cm^2 for 20 mV and 0.68 Ω cm^2 for 50 mV. From these results it seems difficult to determine which modification has the least influence on cell stability, but when we relate the results of both resistances of after-transient cells to that of pristine cells (R_o = 0.13 Ω cm^2, R_p = 0.39 Ω cm^2), it can be clearly determined which transient or cycling thermochemical test influences the stability of PNC73 cells but the
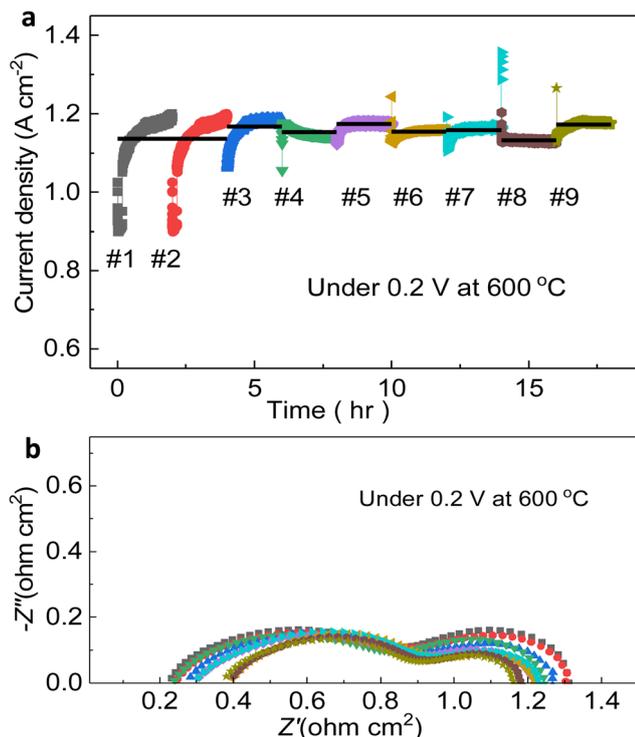
Fig. 6 Stability test at constant voltage and temperature: (a) current density *versus* time curves – constant voltage tests of the PNC73 full cell for 18 h at 0.2 V and 600 °C. (b) EIS curves – constant voltage tests of the PNC73 full cell for 18 h at 0.2 V and 600 °C. For (a) and (b), each curve stands for 2-hour operation.

Fig. 7 Thermal cycling examination: (a) I–V comparisons for 600 °C and 500 °C during the thermal cycling test. (b) EIS comparisons at 600 °C and 500 °C during the thermal cycling test.

cells still function smoothly regardless of the degraded performance. Overall, when evaluating the constant step-voltage test, first transient test, and second transient test as a sequence of tests to assess the durability of PNC73 cells, it becomes evident that the critical electrochemical performance, specifically the current density, is prone to decrease unsubstantially between any two tests, including initial values as comparison. For instance, the current density at 0.6 V for the constant step-voltage test varied between 0.49 A cm^{-2} and 0.79 A cm^{-2}. Similarly, during the first transient test and second transient test, the current density ranged from 0.44 A cm^{-2} to 0.54 A cm^{-2} and 0.45 A cm^{-2} to 0.54 A cm^{-2}, respectively. However, the unanimous de-escalating performance of full cells is subjected to the working lifetime of any random cell. With the stabilized dropping range of 0.10 A cm^{-2}–0.30 A cm^{-2}, the PNC73 cells undoubtedly show durability under collective transient tests.

After these cyclic tests, an constant-voltage stability test was performed to collect the EIS spectra for comparing the evolving cell status. The temperature and voltage were set as 600 °C and 0.2 V. Taking two hours period as a cycle, by the comparison of nine ones, evidently, the current densities are all approximately at the same level, around 1.15 A cm^{-2}, and no abrupt downfall of performance occurred. More importantly, the current density can achieve up to 1.17 A cm^{-2}, which is clearly witnessed. Although there are countable outliers existing, larger or smaller than the mean value, the cell is in its overall stable condition.
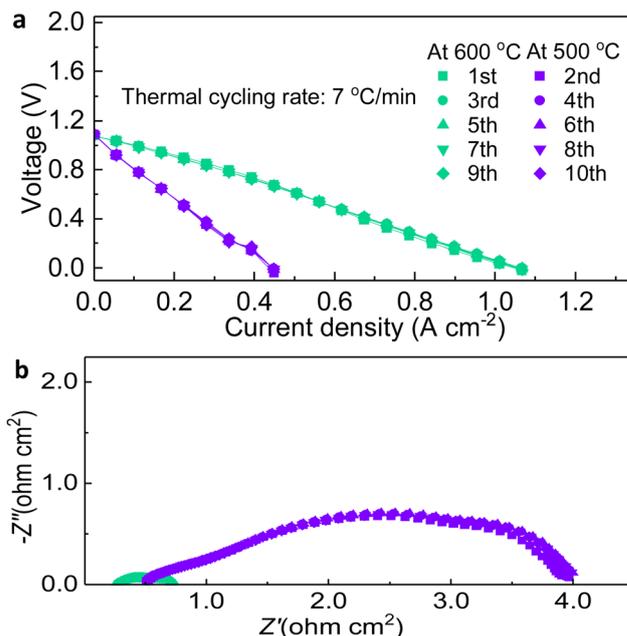
As impedance spectra can reveal (Fig. 6b), specifically, R_o and R_p of each cycle varied a little from others, gathering around 0.25 Ω cm^2 and 1.23 Ω cm^2 respectively, indicating the complicated dynamic status of the cell during the test. Only during last three periods, when the testing duration was between 12 and 18 hours, R_p mildly dropped (less than 10%), which might be explained by the enhanced triple-conducting path and the comparatively flawless gas environment to ensure the HOR and ORR with high-grade chemical kinetics.[57–59]

The thermal cycling resistance was examined by measuring I–V curves between 600 °C and 500 °C 10 times. Immediately after reaching the temperature point, the cell was scanned and the OCV at both temperatures reached around 1.10 V, proving that the fabrication and sealing are long-lasting for the varying temperature, as shown in Fig. 7.[34] The result indicated that the I–V curves have very little variation among them as they are mostly overlapped. After excluding extraneous experimental conditions such as voltage, and when the temperature, which has been shown to have the dominant effect on cell performance, was used as a variable, a stable and certain current density, even the peak power density, has been achieved, which is the corroboration on the stability of PNC73/BZCYYb/NiO-BZCYYb fabricated cells.

Conclusions

Multiple electrochemical tests have been conducted in terms of chemical kinetics and thermodynamics, from constant step-voltage tests to transient cycling tests, and then to thermal cycle tests at different temperatures, to successfully verify the durability of the cell using PNC73 as the cathode material and

BZCYYb as the electrolyte in the fuel cell operation. As demonstrated in various accelerated stress tests, the responses are complicated with some deteriorations during the dynamic operation, which are shown to be oxygen starvation or temporary unstable reaction kinetics. The step voltages or transient voltages lead to a dynamic reaction, mass/charge transfer, and interface evolution, which challenge the cell performances. The thermal cycles have not caused any degradation, and are attributed to the optimization of thermal expansion *via* composition adjustment of the Ni-doped praseodymium cobaltite oxides. As a triple conducting electrode, the PNC73 integrated PCFC is promising to be regarded as a stable and active material system for the application.

Experimental methods

Materials synthesis and characterization

The combinational glycine-citrate combustion approach was used to synthesize PNC73 powder for oxygen electrodes with citric acid and glycine acting as complexing agents in parallel. Stoichiometric quantities of $Pr(NO_3)_3 \cdot 6H_2O$ (99.9%, Alfa Aesar), $Ni(NO_3)_3 \cdot 6H_2O$ (99.9985%, Alfa Aesar), $Co(NO_3)_3 \cdot 6H_2O$ (98+%, Alfa Aesar) and deionized water were dissolved with glycine and citric acid to prepare transparent precursor solution by using ammonia to adjust the pH value close to 7. The chelation agents were added at a molar ratio of glycine : citric acid : cations = 1 : 1.5 : 1, with a cation concentration of 0.02 mol L^{-1}. The initial precursor solution was subsequently heated while being stirred magnetically for hours. Once the viscous gel was formed, it was then subjected to additional heating at around 200 °C to achieve self-ignition. Ultimately, the gel turned to be a substantial amount of powdery ash. After being transported to a muffle furnace for calcination at a temperature of 1000 °C for 5 hours, the product was finally formed as a crystalline perovskite phase. The electrolyte powder, $BaCe_{0.4}Zr_{0.4}Y_{0.1}Yb_{0.1}O_{3-\delta}$ (BCZYYb4411), was synthesized using a solid-state reaction (SSR) method. The stoichiometric amounts of raw chemicals $BaCO_3$ (99.8%, Alfa Aesar), ZrO_2 (99.9%, Alfa Aesar), CeO_2 (99.9%, Alfa Aesar), Y_2O_3 (99.9%, Alfa Aesar), and Yb_2O_3 (99.9%, Alfa Aesar) were weighed and mixed in ethanol for ball-milling in planetary patterns at 300 rpm for 24 h. The powder product was then dried in an oven and calcined at 1000 °C for 5 h in the muffle furnace to form the perovskite phase.

The crystalline phase structures of both PNC73 powder and BCZYYb4411 powder were examined by X-ray diffraction (XRD, Rigaku SmartLab). Utilizing ESEM analysis (TFS Quattro S) in a secondary electron mode, the morphology of both the whole cell structure and the post-test cell structure was assessed, with a particular emphasis on the cross-sectional view.

Fabrication of full cells

The NiO/BCZYYb4411 hydrogen electrode and electrolyte green tapes were first made using the tape casting process in order to prepare the full cells. Half-cell green tapes were made by laminating the electrode support and electrolyte membrane layers together at 70 °C for 5 hours. After being removed off the tapes, the cells were pre-sintered at 920 °C to eliminate the organic solvents and binder. The half-cell diameter was 1.27 cm before sintering. Finally, the electrolyte was densified by sintering the cells at 1500 °C for 5 hours. The last step in producing complete cells with an active area of 0.178 cm^2 was to fire the PNC electrode onto the electrolyte at 1000 °C for 5 hours for a good mechanical adhesion.

Electrochemical measurements and data acquisition

To conduct a series of electrochemical tests, the button cell, as it was originally fabricated, was securely glued and sealed onto the testing fixture using a ceramic sealant (Ceramabond 552) for the curing process before the test. During fuel cell mode testing, the PNC oxygen electrode was exposed to atmospheric air, while the fuel electrode was supplied with a flow of H_2 gas containing 3% steam at a rate of 20 mL min^{-1}. Once the reduction process was fully complete and a steady open circuit voltage (OCV) was achieved at the desired temperature (600 °C), current–voltage characteristic curves, impedance spectra at OCV with frequency ranging from 10^5 Hz to 0.1 Hz and stability tests within transient or dynamic cycling patterns were recorded by an electrochemical working station (Gamry Interface 5000E). The constant step-voltage test was performed at 600 °C, with output voltages ranging from 0.8 V to 0.4 V in 17 sections, each with a step size of 0.2 V. The transient cycling tests were performed within the voltage range of 0.8 V to 0.2 V for 100 cycles, operating in the fuel cell mode at a temperature of 600 °C. The as-fabricated full cell underwent second transient cycling tests in the fuel cell mode at 600 °C. The tests consisted of 100 cycles from 0.9 V to 0.2 V, with step-voltages of 20 mV, 50 mV, and 100 mV. The PNC73 cells were then tested for a constant-voltage durability test, where the cells were subjected to an output voltage of 0.2 V for a total of 9 cycles, each lasting 2 hours. The thermal cycling test was performed by alternating the temperature between 600 °C and 500 °C, with a shift of 100 °C within every 15 minutes. All data were collected and analyzed using Gamry Framework Software.

Author contributions

WB and HD conceptualized the work and methodology. SZ prepared the samples, performed SEM measurements with data analysis, and conducted all electrochemical tests. HD supervised the project and acquired funding. All authors contributed to the writing of the original draft and the review.

Conflicts of interest

There are no conflicts to declare.

Acknowledgements

References

1 Y. Wang, Y. Ling, B. Wang, G. Zhai, G. Yang, Z. Shao, R. Xiao and T. Li, A Review of Progress in Proton Ceramic Electrochemical Cells: Material and Structural Design, Coupled with Value-Added Chemical Production, *Energy Environ. Sci.*, 2023, **16**(12), 5721–5770.

2 S. Uhm and Y. D. Kim, Electrochemical Conversion of Carbon Dioxide in a Solid Oxide Electrolysis Cell, *Curr. Appl. Phys.*, 2014, **14**(5), 672–679.

3 X. Liu, G. Liu, J. Xue, X. Wang and Q. Li, Hydrogen as a Carrier of Renewable Energies toward Carbon Neutrality: State-of-the-Art and Challenging Issues, *Int. J. Miner., Metall. Mater.*, 2022, **29**(5), 1073–1089.

4 F. Liu, D. Ding and C. Duan, Protonic Ceramic Electrochemical Cells for Synthesizing Sustainable Chemicals and Fuels, *Adv. Sci.*, 2023, **10**(8), 2206478.

5 S. Giddey, S. P. S. Badwal, A. Kulkarni and C. Munnings, A Comprehensive Review of Direct Carbon Fuel Cell Technology, *Prog. Energy Combust. Sci.*, 2012, **38**(3), 360–399.

6 X. Shusheng, S. Qiujie, G. Baosheng, Z. Encong and W. Zhankuan, Research and Development of On-Board Hydrogen-Producing Fuel Cell Vehicles, *Int. J. Hydrogen Energy*, 2020, **45**(35), 17844–17857.

7 L. Duan, K. Huang, X. Zhang and Y. Yang, Comparison Study on Different SOFC Hybrid Systems with Zero-CO_2 Emission, *Energy*, 2013, **58**, 66–77.

8 A. Dubois, S. Ricote and R. J. Braun, Benchmarking the Expected Stack Manufacturing Cost of next Generation, Intermediate-Temperature Protonic Ceramic Fuel Cells with Solid Oxide Fuel Cell Technology, *J. Power Sources*, 2017, **369**, 65–77.

9 C. Duan, J. Tong, M. Shang, S. Nikodemski, M. Sanders, S. Ricote, A. Almansoori and R. O'Hayre, Readily Processed Protonic Ceramic Fuel Cells with High Performance at Low Temperatures, *Science*, 2015, **349**(6254), 1321–1326.

10 C. Duan, J. Huang, N. Sullivan and R. O'Hayre, Proton-Conducting Oxides for Energy Conversion and Storage, *Appl. Phys. Rev.*, 2020, **7**(1), 011314.

11 R. O'Hayre, N. Sullivan, R. Kee, R. Braun, H. Ghezel-Ayagh, E. Tang and M. Pastula, *Low-Cost Intermediate-Temperature Fuel-Flexible Protonic-Ceramic Fuel Cell and Stack*, Technical Report, DOE-CSM-0493-1, 2021, 1861417, DOI: **10.2172/ 1861417**.

12 J. Dailly, M. Ancelin and M. Marrony, Long Term Testing of BCZY-Based Protonic Ceramic Fuel Cell PCFC: Micro-Generation Profile and Reversible Production of Hydrogen and Electricity, *Solid State Ionics*, 2017, **306**, 69–75.

13 J. Cao, Y. Ji and Z. Shao, Perovskites for Protonic Ceramic Fuel Cells: A Review, *Energy Environ. Sci.*, 2022, **15**(6), 2200–2232.

14 R. O'Hayre, N. Sullivan, R. Kee, R. Braun, H. Ghezel-Ayagh, E. Tang and M. Pastula, *Low-Cost Intermediate-Temperature Fuel-Flexible Protonic-Ceramic Fuel Cell and Stack*, Technical Report, DOE-CSM-0493-1, 2021, 1861417, DOI: **10.2172/ 1861417**.

15 C. Duan, R. J. Kee, H. Zhu, C. Karakaya, Y. Chen, S. Ricote, A. Jarry, E. J. Crumlin, D. Hook, R. Braun, N. P. Sullivan and R. O'Hayre, Highly Durable, Coking and Sulfur Tolerant, Fuel-Flexible Protonic Ceramic Fuel Cells, *Nature*, 2018, **557**(7704), 217–222.

16 S. Choi, C. J. Kucharczyk, Y. Liang, X. Zhang, I. Takeuchi, H.-I. Ji and S. M. Haile, Exceptional Power Density and Stability at Intermediate Temperatures in Protonic Ceramic Fuel Cells, *Nat. Energy*, 2018, **3**(3), 202–210.

17 D. Cao, M. Zhou, X. Yan, Z. Liu and J. Liu, High Performance Low-Temperature Tubular Protonic Ceramic Fuel Cells Based on Barium Cerate-Zirconate Electrolyte, *Electrochem. Commun.*, 2021, **125**, 106986.

18 W. Zhang and Y. H. Hu, Progress in Proton-conducting Oxides as Electrolytes for Low-temperature Solid Oxide Fuel Cells: From Materials to Devices, *Energy Sci. Eng.*, 2021, **9**(7), 984–1011.

19 C. Duan, J. Tong, M. Shang, S. Nikodemski, M. Sanders, S. Ricote, A. Almansoori and R. O'Hayre, Readily Processed Protonic Ceramic Fuel Cells with High Performance at Low Temperatures, *Science*, 2015, **349**(6254), 1321–1326.

20 H. Li, J. Li, X. Wang, C. Xie, Y. Wang and X. Ding, Electrochemical Performance and Enhancement of Hydration Kinetics on $BaCo_{0.7}Fe_{0.2}Zr_{0.1}O_{3-\delta}$ Cathode for Protonic Ceramic Fuel Cells, *ACS Appl. Energy Mater.*, 2023, **6**(17), 8966–8975.

21 W. Bian, W. Wu, Y. Gao, J. Y. Gomez, H. Ding, W. Tang, M. Zhou and D. Ding, Regulation of Cathode Mass and Charge Transfer by Structural 3D Engineering for Protonic Ceramic Fuel Cell at 400 °C, *Adv. Funct. Mater.*, 2021, **31**(33), 2102907.

22 Z. Li, Q. He, L. Xia, Q. Xu, C. Cheng, J. Wang and M. Ni, Effects of Cathode Thickness and Microstructural Properties on the Performance of Protonic Ceramic Fuel Cell (PCFC): A 3D Modelling Study, *Int. J. Hydrogen Energy*, 2022, **47**(6), 4047–4061.

23 S. Hu, J. Li, Y. Zeng, J. Pu and B. Chi, A Mini Review of the Recent Progress of Electrode Materials for Low-Temperature Solid Oxide Fuel Cells, *Phys. Chem. Chem. Phys.*, 2023, **25**(8), 5926–5941.

24 M. Li, K. Chen, B. Hua, J. Luo, W. D. A. Rickard, J. Li, J. T. S. Irvine and S. P. Jiang, Smart Utilization of Cobaltite-Based Double Perovskite Cathodes on Barrier-Layer-Free Zirconia Electrolyte of Solid Oxide Fuel Cells, *J. Mater. Chem. A*, 2016, **4**(48), 19019–19025.

25 A. Yan, M. Cheng, Y. Dong, W. Yang, V. Maragou, S. Song and P. Tsiakaras, Investigation of a $Ba_{0.5}Sr_{0.5}Co_{0.8}Fe_{0.2}O_{3-\delta}$ Based Cathode IT-SOFC, *Appl. Catal., B*, 2006, **66**(1–2), 64–71.

26 H. Qi, Z. Zhao, B. Tu and M. Cheng, Reaction Tuned Formation of Hierarchical $BaCo_{0.4}Fe_{0.4}Zr_{0.1}Y_{0.1}O_{3-\delta}$ Cathode, *J. Power Sources*, 2020, **455**, 227971.

27 C. Kim, H. Lee, I. Jang, S. Kim, H. Jung, M. Ryu, J. Kim, D. Lee, H. Yoon, U. Paik and T. Song, $BaCo_{0.4}Fe_{0.4}Zr_{0.1}Y_{0.1}O_{3-\delta}$ Triple Conductor for Boosting Electrode Efficiency for Proton Conducting Fuel Cells, *Int. J. Hydrogen Energy*, 2022, **47**(8), 5499–5506.

28 J. Li, J. Hou, Y. Lu, Q. Wang, X. Xi, Y. Fan, X.-Z. Fu and J.-L. Luo, Ca-Containing $Ba_{0.95}Ca_{0.05}Co_{0.4}Fe_{0.4}Zr_{0.1}Y_{0.1}O_{3-\delta}$ Cathode with High CO_2-Poisoning Tolerance for Proton-Conducting Solid Oxide Fuel Cells, *J. Power Sources*, 2020, **453**, 227909.

29 Q. Wang, J. Hou, Y. Fan, X. Xi, J. Li, Y. Lu, G. Huo, L. Shao, X.-Z. Fu and J.-L. Luo, $Pr_2BaNiMnO_{7-\delta}$ Double-Layered Ruddlesden–Popper Perovskite Oxides as Efficient Cathode Electrocatalysts for Low Temperature Proton Conducting Solid Oxide Fuel Cells, *J. Mater. Chem. A*, 2020, **8**(16), 7704–7712.

30 P. Li, R. Dong, R. Wang, T. Shao, F. Yan, P. Zhang, D. Fu and R. Wang, The Performance of Ruddlesden–Popper (R-P) Structured $Pr_{2-x}Sr_xNi_{0.2}Mn_{0.8}O_4$ for Reversible Single-Component Cells. *ACS Sustainable*, *Chem. Eng.*, 2021, **9**(40), 13582–13594.

31 S. Chaianansutcharit, K. Hosoi, J. Hyodo, Y.-W. Ju and T. Ishihara, Ruddlesden Popper Oxides of $LnSr_3Fe_3O_{10-\delta}$ (Ln = La, Pr, Nd, Sm, Eu, and Gd) as Active Cathodes for Low Temperature Solid Oxide Fuel Cells, *J. Mater. Chem. A*, 2015, **3**(23), 12357–12366.

32 Y. Alizad Farzin, M. Bjerg Mogensen, S. Pirou and H. Lund Frandsen, *Perovskite/Ruddlesden–Popper Composite Fuel Electrode of Strontium-Praseodymium-Manganese Oxide for Solid Oxide Cells: An Alternative Candidate*, 2023.

33 W. Tang, H. Ding, W. Bian, C. Y. Regalado Vera, J. Y. Gomez, Y. Dong, J. Li, W. Wu, W. Fan, M. Zhou, C. Gore, B. M. Blackburn, H. Luo and D. Ding, An Unbalanced Battle in Excellence: Revealing Effect of Ni/Co Occupancy on Water Splitting and Oxygen Reduction Reactions in Triple-Conducting Oxides for Protonic Ceramic Electrochemical Cells, *Small*, 2022, **18**(30), 2201953.

34 W. Bian, W. Wu, B. Wang, W. Tang, M. Zhou, C. Jin, H. Ding, W. Fan, Y. Dong, J. Li and D. Ding, Revitalizing Interface in Protonic Ceramic Cells by Acid Etch, *Nature*, 2022, **604**(7906), 479–485.

35 H. Wang, G. Li, X. Guan, M. Zhao and L. Li, Lightly Doping Ca^{2+} in Perovskite $PrCoO_3$ for Tailored Spin States and Electrical Properties, *Phys. Chem. Chem. Phys.*, 2011, **13**(39), 17775.

36 Y. Chen, W. Zhou, D. Ding, M. Liu, F. Ciucci, M. Tade and Z. Shao, Advances in Cathode Materials for Solid Oxide Fuel Cells: Complex Oxides without Alkaline Earth Metal Elements, *Adv. Energy Mater.*, 2015, **5**(18), 1500537.

37 Y. Li, W. Zhang, Y. Zheng, J. Chen, B. Yu, Y. Chen and M. Liu, Controlling Cation Segregation in Perovskite-Based Electrodes for High Electro-Catalytic Activity and Durability, *Chem. Soc. Rev.*, 2017, **46**(20), 6345–6378.

38 Y. Chen, Y. Choi, S. Yoo, Y. Ding, R. Yan, K. Pei, C. Qu, L. Zhang, I. Chang, B. Zhao, Y. Zhang, H. Chen, Y. Chen, C. Yang, B. deGlee, R. Murphy, J. Liu and M. Liu, A Highly

39 Efficient Multi-Phase Catalyst Dramatically Enhances the Rate of Oxygen Reduction, *Joule*, 2018, **2**(5), 938–949.

39 S. J. Kim, T. Akbay, J. Matsuda, A. Takagaki and T. Ishihara, Strain Effects on Oxygen Reduction Activity of Pr_2NiO_4 Caused by Gold Bulk Dispersion for Low Temperature Solid Oxide Fuel Cells, *ACS Appl. Energy Mater.*, 2019, **2**(2), 1210–1220.

40 H. Ding, W. Wu, C. Jiang, Y. Ding, W. Bian, B. Hu, P. Singh, C. J. Orme, L. Wang, Y. Zhang and D. Ding, Self-Sustainable Protonic Ceramic Electrochemical Cells Using a Triple Conducting Electrode for Hydrogen and Power Production, *Nat. Commun.*, 2020, **11**(1), 1907.

41 H.-S. Noh, J. Hong, H. Kim, K. J. Yoon, B.-K. Kim, H.-W. Lee, J.-H. Lee and J.-W. Son, Scale-Up of Thin-Film Deposition-Based Solid Oxide Fuel Cell by Sputtering, a Commercially Viable Thin-Film Technology, *J. Electrochem. Soc.*, 2016, **163**(7), F613–F617.

42 H. Nirasawa, Current Status of National SOFC Projects in Japan, *ECS Trans.*, 2017, **78**(1), 33–40.

43 C. Mendonça, A. Ferreira and D. M. F. Santos, Towards the Commercialization of Solid Oxide Fuel Cells: Recent Advances in Materials and Integration Strategies, *Fuels*, 2021, **2**(4), 393–419.

44 M. Y. Park, S.-Y. Park, H. Seo, J.-M. Jung, H. K. Hwang, J. Hong, J.-Y. Park, I. Lee and K. J. Yoon, Construction of High-Temperature Electronic Conduction Paths for the Scale-up of Solid Oxide Fuel Cell Technology, *J. Mater. Chem. A*, 2022, **10**(22), 11917–11925.

45 P. Leone and A. Lanzini, Experimental Modeling of Transients in Large SOFC Systems, *J. Fuel Cell Sci. Technol.*, 2013, **10**(1), 011004.

46 M. A. Azizi and J. Brouwer, Progress in Solid Oxide Fuel Cell-Gas Turbine Hybrid Power Systems: System Design and Analysis, Transient Operation, Controls and Optimization, *Appl. Energy*, 2018, **215**, 237–289.

47 D. Bhattacharyya and R. Rengaswamy, A Review of Solid Oxide Fuel Cell (SOFC) Dynamic Models, *Ind. Eng. Chem. Res.*, 2009, **48**(13), 6068–6086.

48 K. P. Adzakpa, K. Agbossou, Y. Dube, M. Dostie, M. Fournier and A. Poulin, PEM Fuel Cells Modeling and Analysis Through Current and Voltage Transient Behaviors, *IEEE Trans. Energy Convers.*, 2008, **23**(2), 581–591.

49 M. Ceraolo, C. Miulli and A. Pozio, Modelling Static and Dynamic Behaviour of Proton Exchange Membrane Fuel Cells on the Basis of Electro-Chemical Description, *J. Power Sources*, 2003, **113**(1), 131–144.

50 Y. Shan and S.-Y. Choe, A High Dynamic PEM Fuel Cell Model with Temperature Effects, *J. Power Sources*, 2005, **145**(1), 30–39.

51 N. Wang, C. Tang, L. Du, R. Zhu, L. Xing, Z. Song, B. Yuan, L. Zhao, Y. Aoki and S. Ye, Advanced Cathode Materials for Protonic Ceramic Fuel Cells: Recent Progress and Future Perspectives, *Adv. Energy Mater.*, 2022, **12**(34), 2201882.

52 N. Ni, S. J. Cooper, R. Williams, N. Kemen, D. W. McComb and S. J. Skinner, Degradation of $(La_{0.6}Sr_{0.4})_{0.95}(Co_{0.2}Fe_{0.8})O_{3-\delta}$ Solid Oxide Fuel Cell Cathodes at the Nanometer Scale

and Below, *ACS Appl. Mater. Interfaces*, 2016, **8**(27), 17360–17370.

53 H. Ding and X. Xue, PrBa$_{0.5}$Sr$_{0.5}$Co$_2$O$_{5+\delta}$ Layered Perovskite Cathode for Intermediate Temperature Solid Oxide Fuel Cells, *Electrochimica Acta*, 2010, **55**(11), 3812–3816.

54 Y. Hsiao, The Degradation of SOFC Electrodes, *Solid State Ionics*, 1997, **98**(1–2), 33–38.

55 P. Tanasini, M. Cannarozzo, P. Costamagna, A. Faes, J. Van Herle, A. Hessler-Wyser and C. Comninellis, Experimental and Theoretical Investigation of Degradation Mechanisms by Particle Coarsening in SOFC Electrodes, *Fuel Cells*, 2009, **9**(5), 740–752.

56 B. Stoeckl, V. Subotić, M. Preininger, H. Schroettner and C. Hochenauer, SOFC Operation with Carbon Oxides: Experimental Analysis of Performance and Degradation, *Electrochim. Acta*, 2018, **275**, 256–264.

57 K. Park, S. Yu, J. Bae, H. Kim and Y. Ko, Fast Performance Degradation of SOFC Caused by Cathode Delamination in Long-Term Testing, *Int. J. Hydrogen Energy*, 2010, **35**(16), 8670–8677.

58 Q. Fang, L. Blum and D. Stolten, Electrochemical Performance and Degradation Analysis of an SOFC Short Stack Following Operation of More than 100,000 Hours, *J. Electrochem. Soc.*, 2019, **166**(16), F1320–F1325.

59 Q. Fang, U. De Haart, D. Schäfer, F. Thaler, V. Rangel-Hernandez, R. Peters and L. Blum, Degradation Analysis of an SOFC Short Stack Subject to 10,000 h of Operation, *J. Electrochem. Soc.*, 2020, **167**(14), 144508.